# Thermal two-phase flow with a phase-field method

Keunsoo Park[a], Maria Fernandino[a,*], Carlos A. Dorao[a]

[a]*Department of Energy and Process Engineering, Norwegian University of Science and Technology, N-7491 Trondheim, Norway*

Corresponding author. Tel: +47 73595352

Email-addresses: keunsoo.park@ntnu.no (K. Park), maria.fernandino@ntnu.no (M. Fernandino), carlos.dorao@ntnu.no (C.A. Dorao)

**Abstract**

Phase field methods have become of great interest for the simulation of droplet and bubble dynamics, moving free interfaces and more recently phase change phenomena. One example is the Navier-Stokes-Korteweg (NSK) equations. With a particular focus on the van der Waals fluid, we present the numerical solution of the NSK system with the energy equation included. The least-squares spectral element formulation with a time-stepping procedure, a high-order continuity approximation and an element-by-element technique is implemented to provide a general and robust solver for the thermal NSK equations. A convergence analysis is conducted to verify our solver. Two numerical examples regarding phase transitions of a droplet and thermocapillary convection are provided to validate our solver.

*Key words*: Phase-field model; Navier-Stokes-Korteweg system; Least-squares method; Spectral element method; Two-phase flows; Phase change

## 1. Introduction

Liquid-vapor two-phase flow occurs in many natural phenomena as well as industrial applications. Particularly the applications of liquid-vapor phase transition are extremely wide, ranging over cavitation, boiling, evaporation and condensation. In industry, phase transition takes place in the fuel injection system, heat exchangers, and various pipelines. During phase transition, mass and heat transfer phenomena through the phase interface are governed by the laws of thermodynamics, and many modeling techniques for the interfacial dynamics are available for these transfer processes.

As opposed to sharp-interface methods, diffuse-interface methods describe the phase interface as a microscopic transition region with continuous variations of physical quantities. The benefits of the diffuse-interface method over other approaches are that there is only one set of PDEs to be solved over the entire domain including the interface area, and the method can handle the complicated topological changes without ad-hoc procedures [1]. Among diffuse-interface methods, the phase-field model, which is based on a convection-diffusion type of equation, can overcome shortcomings in the interface tracking methods such as volume of fluids or level-set method by avoiding the interface smearing problems and improving accuracy of surface tension computation [2]. The phase-field methods have been widely used to simulate the flow of two or more fluids such as spinodal decomposition [3-4], head-on droplet collision [5-6], dendritic growth [7] and cancerous tumor growth [8].

The Navier-Stokes-Korteweg (NSK) equations are one of the most popular phase-field models to date. Korteweg proposed a constitutive law for the capillary stress formulation and coupled the van der Waals fluid model with hydrodynamics, yielding the NSK equations [9]. Later, the interstitial working term was introduced into the energy equation to satisfy the second law of thermodynamics [10]. Owing to the thermodynamically consistent nature, the NSK equations have been expected to provide a unified predictive capability for the thermal phenomena. Onuki [11] has showed that the NSK equations may accommodate effects of wetting and heating of a plane solid wall.

However, numerical methods for the thermal NSK equations are faced with stability and accuracy issues. The NSK equations are third-order PDEs due to the expression of the surface tension effect. Another feature of the NSK system is a non-monotone constitutive relation for the pressure, corresponding to a non-convex local part of the energy. As can be seen from Figure 1, there is an unphysical region of negative compressibility in phase transition, denoted as the phase mixture (PM) region. The non-convex energy function results in a mixed hyperbolic-elliptic characteristic of the NSK equations below the critical temperature. Pecenko et al. [4,12] used a transformation of variable for the isothermal case, but it is discarded in the thermal case since it leads to a prohibitive increase in the complexity of the governing equations, and also restricts the range of applicability of the method by increasing the number of constraints on the physical parameter of the fluid. More recently, Liu et al. [13] adapted the entropy variable with an isogeometric analysis, and Tian et al. [14] added Lax-Friedrich terms for the conservative scheme. However, Diehl et al. [15] and Giesselmann et al. [16] pointed out that adding these terms generates parasitic currents at the interface, and these can be removed when the pressure and the Korteweg terms are discretized in a non-conservative fashion.

In the present work, the formulation of [17] for the isothermal NSK equations is extended to the thermal case. Besides the isothermal NSK equations, in the thermal NSK equations, a highly non-linear equation for the total energy is coupled with the mass and momentum conservation equations, and the dependency of the pressure on the temperature is added. The least-squares formulation with $C^1$ Hermite approximation is implemented. The idea of this formulation to the NSK equations is to rewrite the original equations as a second order system, and then apply the spectral element method with $C^1$ continuity to this second order system. The least-squares spectral element method has several desirable numerical properties: (1) it always provides symmetric positive definite system even for non-self-adjoint operators; (2) it circumvents compatibility requirements between approximating function spaces such as the LBB condition; (3) the use of higher continuity discretization improves the approximation accuracy of solution at the phase interface. Additionally, in our solver a space-time coupled formulation and an element-by-element technique are used to handle a long-term of solution evolution. The generality and robustness of the least-squares formulation with high order approximation are demonstrated by showing that it can cope with highly complicated energy equation in the thermal NSK system. We provide the verification and validation of our solver for the thermal NSK equations. To the author's best knowledge, this is the first work of applying the least-squares method into the thermal NSK system.

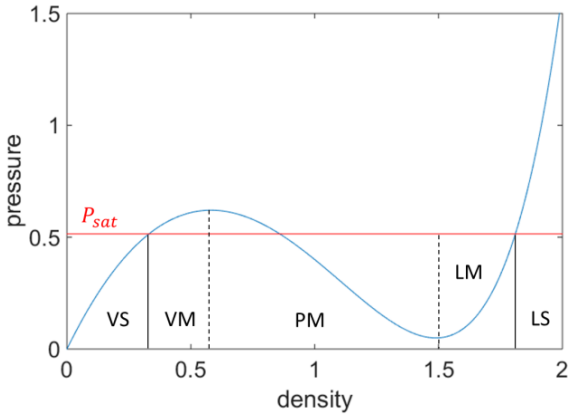


Figure 1. Dimensionless equation of state for van der Waals isothermal fluid at 0.85 of temperature. $P_{sat}$ saturation pressure, VS vapor stable, VM vapor metastable, PM Phase mixture, LM liquid metastable, and LS liquid stable.

The rest of this paper is organized as follows. Section 2 presents a derivation and a formulation of the thermal NSK equations and their nondimensionalization process. In Section 3, the least-squares spectral element method for the governing equations is described. A convergence analysis of our numerical solver can be found in Section 4. Two numerical examples, evaporation/condensation of a bubble and thermocapillary convection, are presented in Section 5. We draw conclusions in Section 6.

## 2. The van der Waals fluid model

### *2.1. Korteweg stress tensor from Helmholtz energy*

The phase-field models are formulated based on their own definitions of the Helmholtz free energy density $\Psi$. For the van der Waals fluid [18], it is given by

$$\Psi(\rho,\theta) = \Psi_{loc}(\rho,\theta) + \frac{K}{2\rho}|\nabla\rho|^2, \tag{2.1}$$

$$\Psi_{loc}(\rho,\theta) = -a\rho + R\theta\log\left(\frac{\rho}{b-\rho}\right) - c\theta\log\left(\frac{\theta}{\theta_0}\right) - d\theta. \tag{2.2}$$

Above, $\Psi_{loc}$ is the local Helmholtz energy density, $\rho$ is the density, $\theta$ is the temperature, $K$ is the capillary coefficient, constants $a$, $b$ and $d$ are the van der Waals constants associated with fluid properties, $c$ is the specific heat capacity, $R$ is the universal gas constant, and $\theta_0$ is a reference temperature.

Mathematically, the equilibrium state in the phase-field method can be found by minimizing a functional of Helmholtz energy $\mathcal{Y}$ over the domain subject to conserving a mass functional $\mathcal{M}$. Those functionals are

$$\mathcal{Y} = \int \rho\Psi dV = \int \left[\rho\Psi_{loc} + \frac{1}{2}K|\nabla\rho|^2\right] dV, \tag{2.3}$$

$$\mathcal{M} = \int \rho dV. \tag{2.4}$$

And it leads to the following Euler-Lagrange equation:

$$K\nabla^2\rho - \frac{\partial(\rho\Psi_{loc})}{\partial\rho} + \lambda = 0, \tag{2.5}$$

where $\lambda$ is the Lagrange multiplier from the constraint of constant mass. Since both functionals $\mathcal{Y}$ and $\mathcal{M}$ are continuous in time and independent of spatial coordinates, a system has a continuous symmetry property. According to Noether's theorem [19-20], for such system there is a corresponding quantity **N** whose value is conserved in time:

$$\begin{aligned} &\nabla \cdot \mathbf{N} = 0, \\ &\text{where } \mathbf{N} = \mathcal{L}\mathbf{I} - \nabla\rho \otimes \frac{\partial \mathcal{L}}{\partial(\nabla\rho)}, \qquad \mathcal{L} = \rho\Psi_{loc} + \frac{1}{2}K|\nabla\rho|^2 - \lambda\rho. \end{aligned} \tag{2.6}$$

Using (2.5), the conserved tensor **N** becomes that

$$\mathbf{N} = \left(-\rho^2\frac{\partial\Psi_{loc}}{\partial\rho} + K\rho\nabla^2\rho + \frac{1}{2}K|\nabla\rho|^2\right)\mathbf{I} - K\nabla\rho \otimes \nabla\rho. \tag{2.7}$$

The first term in **N** is defined as the thermodynamic pressure as

$$P = \rho^2\frac{\partial\Psi_{loc}}{\partial\rho} = Rb\frac{\rho\theta}{b-\rho} - a\rho^2, \tag{2.8}$$

and the rest of the terms are referred to as the Korteweg stress tensor $\boldsymbol{\varsigma}$:

$$\boldsymbol{\varsigma} = \left(K\rho\nabla^2\rho + \frac{1}{2}K|\nabla\rho|^2\right)\mathbf{I} - K\nabla\rho \otimes \nabla\rho. \tag{2.9}$$

Meanwhile, the internal energy $e$ can be defined from of $\Psi$ as

$$e = \Psi_{loc} - \theta\frac{\partial\Psi_{loc}}{\partial\theta} = c\theta - a\rho, \tag{2.10}$$

and the interfacial energy and the kinetic energy are included into the formulation of the total energy $\mathcal{E}$ as

$$\mathcal{E} = \rho\left(e + \frac{1}{2}|\boldsymbol{u}|^2\right) + \frac{1}{2}K|\nabla\rho|^2, \tag{2.11}$$

*2.2. The thermal Navier-Stokes-Korteweg system*

We define the space-time set $\Omega := \Omega_{\boldsymbol{x}} \times (0,T), T > 0$, for a two-dimensional open domain $\Omega_{\boldsymbol{x}} \subset \mathbb{R}^2$. The spatial boundary of $\Omega$ is denoted as $\Gamma := \partial\Omega_{\boldsymbol{x}} \times (0,T)$, and the unit outward normal vector to $\Gamma$ is denoted as $\boldsymbol{n}$. For a thermal flow with compressible and viscous two-phase fluids, the thermal Naiver-Stokes-Korteweg (NSK) problem with initial/boundary conditions can be state as follows: find the unknowns $\rho = \rho(\boldsymbol{x},t): \Omega \to (0,b)$, $\boldsymbol{u} = \boldsymbol{u}(\boldsymbol{x},t): \Omega \to \mathbb{R}^2$, and $\theta = \theta(\boldsymbol{x},t): \Omega \to \mathbb{R}$ such that

$$\frac{\partial\rho}{\partial t} + \nabla \cdot (\rho\boldsymbol{u}) = 0 \quad \text{in } \Omega, \tag{2.12}$$

$$\frac{\partial(\rho \boldsymbol{u})}{\partial t} + \nabla \cdot (\rho \boldsymbol{u} \otimes \boldsymbol{u}) + \nabla P - \nabla \cdot \boldsymbol{\tau} - \nabla \cdot \boldsymbol{\varsigma} = 0 \quad \text{in } \Omega, \tag{2.13}$$

$$\frac{\partial \mathcal{E}}{\partial t} + \nabla \cdot [(\mathcal{E} + P)\boldsymbol{u}] - \nabla \cdot [(\boldsymbol{\tau} + \boldsymbol{\varsigma})\boldsymbol{u}] + \nabla \cdot \boldsymbol{q} + \nabla \cdot \boldsymbol{\Pi} = 0 \quad \text{in } \Omega, \tag{2.14}$$

$$\nabla \rho \cdot \boldsymbol{n} = 0 \quad \text{on } \Gamma, \tag{2.15}$$

$$\rho(\boldsymbol{x}, 0) = \rho_0(\boldsymbol{x}) \quad \text{in } \Omega_{\boldsymbol{x}}, \tag{2.16}$$

$$\boldsymbol{u}(\boldsymbol{x}, 0) = \boldsymbol{u}_0(\boldsymbol{x}) \quad \text{in } \Omega_{\boldsymbol{x}}, \tag{2.17}$$

$$\theta(\boldsymbol{x}, 0) = \theta_0(\boldsymbol{x}) \quad \text{in } \Omega_{\boldsymbol{x}}, \tag{2.18}$$

together with proper boundary conditions for $\boldsymbol{u}$ and $\theta$. $\mathcal{E}$ can be expressed as a function of $\theta$ based on its definition presented in (2.10)-(2.11). Here, $\rho_0 : \Omega \to (0, b)$, $\boldsymbol{u}_0 : \Omega \to \mathbb{R}^2$ and $\theta_0 : \Omega \to \mathbb{R}$ are given for the initial conditions. $\boldsymbol{\tau}$ is the viscous stress tensor for a Newtonian fluid, $\boldsymbol{q}$ is the heat, and $\boldsymbol{\Pi}$ is the interstitial working flux are described as

$$\boldsymbol{\tau} = \mu(\nabla \boldsymbol{u} + \nabla \boldsymbol{u}^T) + \nu(\nabla \cdot \boldsymbol{u})\mathbf{I}, \tag{2.19}$$

$$\boldsymbol{q} = -k \nabla \theta, \tag{2.20}$$

$$\boldsymbol{\Pi} = K\rho(\nabla \cdot \boldsymbol{u}) \nabla \rho, \tag{2.21}$$

where $\mu$ and $\nu$ are the first and second viscosity coefficient, and $k$ is the thermal conductivity. Here, a choice of $\mu > 0$ and $\nu = -2\mu/3$ is adopted based on the Stokes assumption. The divergence of the Korteweg stress tensor $\boldsymbol{\varsigma}$ can be simplified as

$$\nabla \cdot \boldsymbol{\varsigma} = K\rho \nabla \cdot (\nabla^2 \rho). \tag{2.22}$$

The first two terms of the momentum conservation equation (2.13) can be rewritten as

$$\frac{\partial(\rho \boldsymbol{u})}{\partial t} + \nabla \cdot (\rho \boldsymbol{u} \otimes \boldsymbol{u}) = \rho \left( \frac{\partial \boldsymbol{u}}{\partial t} + \boldsymbol{u} \cdot \nabla \boldsymbol{u} \right) + \boldsymbol{u} \left[ \frac{\partial \rho}{\partial t} + \nabla \cdot (\rho \boldsymbol{u}) \right]. \tag{2.23}$$

The terms in the square brackets is equal to the terms in the left-hand side of the continuity equation (2.12); hence they become zero. Thus, (2.13) reduces to

$$\rho \left( \frac{\partial \boldsymbol{u}}{\partial t} + \boldsymbol{u} \cdot \nabla \boldsymbol{u} \right) + \nabla P - \nabla \cdot \boldsymbol{\tau} - \nabla \cdot \boldsymbol{\varsigma} = 0. \tag{2.24}$$

### *2.3. Dimensionless form of the governing equations*

The non-dimensionalization of the thermal NSK equations can be performed with the following reference variables denoted with a subscript 0 and the non-dimensional quantities denoted with a superscript *:

$$\boldsymbol{x}^* = \frac{\boldsymbol{x}}{L_0}, \boldsymbol{u}^* = \frac{\boldsymbol{u}}{U_0}, \rho^* = \frac{\rho}{\rho_0}, P^* = \frac{P}{P_0}, \theta^* = \frac{\theta}{\theta_0}, \mathcal{E}^* = \frac{\mathcal{E}}{\mathcal{E}_0}, \boldsymbol{q}^* = \frac{\boldsymbol{q}}{q_0}, \boldsymbol{\Pi}^* = \frac{\boldsymbol{\Pi}}{\Pi_0} \tag{2.25}$$

We set the reference values of the density, pressure and temperature as their critical values in the van der Waals fluid model:

$$\rho_0 = \rho_c = \frac{b}{3}, \quad P_0 = P_c = \frac{ab^2}{27}, \quad \theta_0 = \theta_c = \frac{8ab}{27R}. \tag{2.26}$$

In this study, the reference velocity is the average sound speed $U_0 = \sqrt{P_0/\rho_0}$, and the reference length is defined as $L_0 = U_0 t_0$ using the reference time $t_0$. With these reference values, the Reynold number $Re$, the Weber number $We$ and the scaled heat conductivity $k_0$ are defined as

$$Re = \frac{\rho_0 U_0 L_0}{\mu}, \quad We = \frac{L_0^2 U_0^2}{K\rho_0} = \frac{\rho_0 U_0^2 L_0}{\sigma}, \quad k_0 = \frac{k\theta_0}{\rho_0 L_0 U_0^3}. \tag{2.27}$$

with $\sigma$ the surface tension. The dimensionless pressure, total energy, heat and interstitial working flux can be expressed as

$$P = \rho_0 U_0^2 \left[\frac{8\rho^*\theta^*}{3-\rho^*} - 3\rho^{*2}\right], \tag{2.28}$$

$$\mathcal{E} = \rho_0 U_0^2 \left[-3\rho^{*2} + c\rho^*\theta^* + \frac{1}{2We}|\nabla^*\rho^*|^2 + \frac{1}{2}\rho^*|\boldsymbol{u}^*|^2\right], \tag{2.29}$$

$$\boldsymbol{q} = -\frac{k\theta_0}{L_0}\nabla^*\theta^*, \tag{2.30}$$

$$\boldsymbol{\Pi} = \frac{K\rho_0^2 U_0}{L_0^2}\rho^*(\nabla^*\cdot\boldsymbol{u}^*)\nabla^*\rho^*. \tag{2.31}$$

With the non-dimensional quantities, the dimensionless form of the balance equations, (2.12), (2.24) and (2.14), the viscous stress tensor and the Korteweg stress tensor can be written as

$$\frac{\rho_0 U_0}{L_0}\left[\frac{\partial\rho^*}{\partial t^*} + \nabla^*\cdot(\rho^*\boldsymbol{u}^*)\right] = 0, \tag{2.32}$$

$$\frac{\rho_0 U_0^2}{L_0}\left[\rho^*\left(\frac{\partial\boldsymbol{u}^*}{\partial t^*} + \boldsymbol{u}^*\cdot\nabla^*\boldsymbol{u}^*\right) + \nabla^*P^* - \frac{1}{Re}\nabla^*\cdot\boldsymbol{\tau}^* - \frac{1}{We}\nabla^*\cdot\boldsymbol{\varsigma}^*\right] = 0, \tag{2.33}$$

$$\frac{\rho_0 U_0^3}{L_0}\left[\frac{\partial\mathcal{E}^*}{\partial t^*} + \nabla^*\cdot[(\mathcal{E}^*+P^*)\boldsymbol{u}^*] - \frac{1}{Re}\nabla^*\cdot(\boldsymbol{\tau}^*\boldsymbol{u}^*) - \frac{1}{We}\nabla^*\cdot(\boldsymbol{\varsigma}^*\boldsymbol{u}^*) + k_0\nabla^*\cdot\boldsymbol{q}^* + \frac{1}{We}\nabla^*\cdot\boldsymbol{\Pi}^*\right] = 0, \tag{2.34}$$

$$\boldsymbol{\tau}^* = \nabla^*\boldsymbol{u}^* + \nabla^*\boldsymbol{u}^{*T} - \frac{2}{3}\nabla^*\cdot\boldsymbol{u}^*\mathbf{I}, \tag{2.35}$$

$$\boldsymbol{\varsigma}^* = \left(\rho^*\nabla^{*2}\rho^* + \frac{1}{2}|\nabla^*\rho^*|^2\right)\mathbf{I} - \nabla^*\rho^* \otimes^* \nabla^*\rho^*. \tag{2.36}$$

In this formulation, pressure is viewed as a dependent variable of the density and temperature. For the thermal case, the derivative of pressure in (2.33) and (2.34) is expressed as

$$\nabla^*P^* = \frac{\partial P^*}{\partial\rho^*}\nabla^*\rho^* + \frac{\partial P^*}{\partial\theta^*}\nabla^*\theta^* = \left[\frac{24}{(3-\rho^*)^2} - 6\rho^*\right]\nabla^*\rho^* + \frac{8\rho^*}{3-\rho^*}\nabla^*\theta^*. \tag{2.37}$$

To allow the use of $C^1$ continuous element expansions in the least-squares finite element formulation, the third-order derivative of the density in the Korteweg stress term needs to be recast as a lower-order derivative term. We define a new variable $\varphi$ to represent the Laplacian of density as

$$\varphi = \nabla^2 \rho. \tag{2.38}$$

Dropping out the subscript *, the dimensionless of the thermal NSK equations in terms of the prior variables and $\varphi$ becomes

$$\frac{\partial \rho}{\partial t} + \nabla \cdot (\rho \boldsymbol{u}) = 0, \tag{2.39}$$

$$\begin{aligned} \rho\left(\frac{\partial \boldsymbol{u}}{\partial t} + \boldsymbol{u} \cdot \nabla \boldsymbol{u}\right) + \left[\frac{24}{(3-\rho)^2} - 6\rho\right]\nabla\rho - \frac{1}{Re}\nabla \cdot \left(\nabla \boldsymbol{u} + \nabla \boldsymbol{u}^T - \frac{2}{3}\nabla \cdot \boldsymbol{u}\mathbf{I}\right) - \frac{1}{We}\rho\nabla\varphi \\ = -\frac{8\rho}{3-\rho}\nabla\theta, \end{aligned} \tag{2.40}$$

$$\begin{aligned} c\rho\left[\frac{\partial \theta}{\partial t} + (\boldsymbol{u} \cdot \nabla)\theta\right] + \frac{8\rho}{3-\rho}(\boldsymbol{u} \cdot \nabla)\theta - k_0\nabla^2\theta + \left[\frac{24}{(3-\rho)^2}\nabla\rho \cdot \boldsymbol{u} + \frac{8\rho}{3-\rho}\nabla \cdot \boldsymbol{u}\right]\theta \\ = \alpha + \beta + \gamma + \delta + \varepsilon, \end{aligned} \tag{2.41}$$

where

$$\begin{aligned} \alpha = -\frac{1}{We}\left[\frac{\partial \rho}{\partial x}\left(\frac{\partial^2 \rho}{\partial x\,\partial t} + u\frac{\partial^2 \rho}{\partial x^2} + v\frac{\partial^2 \rho}{\partial x\,\partial y}\right) + \frac{\partial \rho}{\partial y}\left(\frac{\partial^2 \rho}{\partial y\,\partial t} + u\frac{\partial^2 \rho}{\partial x\,\partial y} + v\frac{\partial^2 \rho}{\partial y^2}\right)\right] \\ - \rho u\left(\frac{\partial u}{\partial t} + u\frac{\partial u}{\partial x} + v\frac{\partial u}{\partial y}\right) - \rho v\left(\frac{\partial v}{\partial t} + u\frac{\partial v}{\partial x} + v\frac{\partial v}{\partial y}\right) - 3\rho^2\left(\frac{\partial u}{\partial x} + \frac{\partial v}{\partial y}\right) \\ - \frac{1}{2We}\left[\left(\frac{\partial \rho}{\partial x}\right)^2 + \left(\frac{\partial \rho}{\partial y}\right)^2\right]\left(\frac{\partial u}{\partial x} + \frac{\partial v}{\partial y}\right), \end{aligned} \tag{2.42}$$

$$\begin{aligned} \beta = -\frac{1}{We}\left[\left(\frac{\partial u}{\partial x} + \frac{\partial v}{\partial y}\right)\left\{\left(\frac{\partial \rho}{\partial x}\right)^2 + \left(\frac{\partial \rho}{\partial y}\right)^2 + \rho\left(\frac{\partial^2 \rho}{\partial x^2} + \frac{\partial^2 \rho}{\partial y^2}\right)\right\}\right. \\ \left. + \rho\left\{\left(\frac{\partial^2 u}{\partial x^2} + \frac{\partial^2 v}{\partial x\,\partial y}\right)\frac{\partial \rho}{\partial x} + \left(\frac{\partial^2 u}{\partial x\,\partial y} + \frac{\partial^2 v}{\partial y^2}\right)\frac{\partial \rho}{\partial y}\right\}\right], \end{aligned} \tag{2.43}$$

$$\begin{aligned} \gamma = \frac{1}{Re}\left[u\left(\frac{4}{3}\frac{\partial^2 u}{\partial x^2} + \frac{1}{3}\frac{\partial^2 v}{\partial x\,\partial y} + \frac{\partial^2 u}{\partial y^2}\right) + v\left(\frac{\partial^2 v}{\partial x^2} + \frac{1}{3}\frac{\partial^2 u}{\partial x\,\partial y} + \frac{4}{3}\frac{\partial^2 v}{\partial y^2}\right) + \frac{4}{3}\left(\frac{\partial u}{\partial x}\right)^2 - \frac{4}{3}\frac{\partial u}{\partial x}\frac{\partial \mathrm{v}}{\partial y}\right. \\ \left. + \left(\frac{\partial u}{\partial y}\right)^2 + \left(\frac{\partial v}{\partial x}\right)^2 + 2\frac{\partial u}{\partial y}\frac{\partial \mathrm{v}}{\partial x} + \frac{4}{3}\left(\frac{\partial v}{\partial y}\right)^2\right], \end{aligned} \tag{2.44}$$

$$\begin{aligned} \delta = \frac{1}{We}\left[\rho u\frac{\partial \varphi}{\partial x} + \rho v\frac{\partial \varphi}{\partial y} + \frac{\partial u}{\partial x}\left\{\rho\varphi - \frac{1}{2}\left(\frac{\partial \rho}{\partial x}\right)^2 + \frac{1}{2}\left(\frac{\partial \rho}{\partial y}\right)^2\right\} - \frac{\partial u}{\partial y}\frac{\partial \rho}{\partial x}\frac{\partial \rho}{\partial y} - \frac{\partial v}{\partial x}\frac{\partial \rho}{\partial x}\frac{\partial \rho}{\partial y}\right] \\ + \frac{\partial v}{\partial y}\left\{\rho\varphi + \frac{1}{2}\left(\frac{\partial \rho}{\partial x}\right)^2 - \frac{1}{2}\left(\frac{\partial \rho}{\partial y}\right)^2\right\}, \end{aligned} \tag{2.45}$$

$$\varepsilon = 6\rho\left(\frac{\partial \rho}{\partial x}u + \frac{\partial \rho}{\partial \mathrm{y}}v\right) + 3\rho^2\left(\frac{\partial u}{\partial x} + \frac{\partial v}{\partial y}\right). \tag{2.46}$$

## 3. The numerical method

### *3.1. Least-squares formulation*

The system (2.36)-(2.39) can be viewed as the coupled Navier-Stokes equations, (2.36)-(2.38), and the energy

equation (2.39). We design the decoupling solver with a relaxation method, and the terms from previous decoupling step are denoted as subscript *n*. To be illustrate, the velocity $u_n$ in the *n*-th decoupling iteration is obtained from the previous iteration $u_{n-1}$, and the one from the second previous iteration $u_{n-2}$, with the relaxation parameter $\omega_{dc}$, i.e., $u_n = \omega_{dc}u_{n-1} + (1-\omega_{dc})u_{n-2}$. The $L^2$-norm least-squares energy functional based on the residuals of the system (2.36)-(2.38) and (2.39) can be written as follows, respectively:

$$\begin{aligned}\mathcal{J}_{NS}(\rho,\boldsymbol{u},\varphi;\theta_n) = \frac{1}{2}\Bigg(&\left\|\frac{\partial\rho}{\partial t}+\nabla\cdot(\rho\boldsymbol{u})\right\|_{0,\Omega}^2 \\ &+\left\|\rho\left(\frac{\partial\boldsymbol{u}}{\partial t}+\boldsymbol{u}\cdot\nabla\boldsymbol{u}\right)+\left[\frac{24}{(3-\rho)^2}-6\rho\right]\nabla\rho-\frac{1}{Re}\nabla\cdot\left(\nabla\boldsymbol{u}+\nabla\boldsymbol{u}^T-\frac{2}{3}\nabla\cdot\boldsymbol{u}\mathbf{I}\right)\right. \\ &\left.-\frac{1}{We}\rho\nabla\varphi+\frac{8\rho}{3-\rho}\nabla\theta_n\right\|_{0,\Omega}^2+\|\nabla^2\rho-\varphi\|_{0,\Omega}^2\Bigg),\end{aligned} \tag{3.1}$$

$$\begin{aligned}\mathcal{J}_E(\theta;\rho_n,\boldsymbol{u}_n,\varphi_n) = \frac{1}{2}\Bigg(&\left\|c\rho_n\left[\frac{\partial\theta}{\partial t}+(\boldsymbol{u}_n\cdot\nabla)\theta\right]+\frac{8\rho_n}{3-\rho_n}(\boldsymbol{u}_n\cdot\nabla)\theta-k_0\nabla^2\theta\right. \\ &\left.+\left[\frac{24}{(3-\rho_n)^2}\nabla\rho_n\cdot\boldsymbol{u}_n+\frac{8\rho_n}{3-\rho_n}\nabla\cdot\boldsymbol{u}_n\right]\theta-\alpha_n-\beta_n-\gamma_n-\delta_n-\varepsilon_n\right\|_{0,\Omega}^2\Bigg),\end{aligned} \tag{3.2}$$

where the subscripts $NS$ and $E$ stand for the Navier-Stokes equations and the energy equation. Let $\mathcal{W}_1$ denote the solution space for $\rho$, $\varphi$ and $\theta$, and let $\mathcal{W}_2$ denote the solution space for $\boldsymbol{u}$. The minimization statement in the least-squares sense for the Navier-Stokes equations can be expressed as

Find $(\rho,\boldsymbol{u},\varphi)\in X_{NS}(\Omega)$ for a given $\theta_n$ such that

$$(\rho,\boldsymbol{u},\varphi) = \underset{(\varrho,\boldsymbol{v},Q)\in X_{NS}}{\operatorname{argmin}}\ \mathcal{J}_{NS}(\varrho,\boldsymbol{v},Q), \tag{3.3}$$

where $X_{NS}(\Omega)$ is the space of admissible functions for the variables in the Navier-Stokes equations

$$\begin{aligned}X_{NS}(\Omega) = \Big\{&(\rho,\boldsymbol{u},\varphi) \\ &\in L^2(\mathcal{W}_1)\cap H^1\big(L^2(\Omega)\big)\times L^2(\mathcal{W}_2)\cap\Big(H^1\big(L^2(\Omega)\big)\Big)^n\times L^2(\mathcal{W}_1)\cap H^1\big(L^2(\Omega)\big)\Big\}.\end{aligned} \tag{3.4}$$

Simultaneously for the energy equation,

Find $\theta\in X_E(\Omega)$ for a given $(\rho_n,\boldsymbol{u}_n,\varphi_n)$ such that

$$\theta = \underset{\psi\in X_E}{\operatorname{argmin}}\,\mathcal{J}_E(\psi), \tag{3.5}$$

where $X_E(\Omega)$ is the space of admissible functions for the variables in the energy equation as

$$X_E(\Omega) = \big\{\theta\in L^2(\mathcal{W}_1)\cap H^1\big(L^2(\Omega)\big)\big\}. \tag{3.6}$$

Equivalently, it is possible to write the necessary condition for the Navier-Stokes equations as

Find $\mathbf{U}_{NS} = (\rho,\boldsymbol{u},\varphi)\in X_{NS}(\Omega)$ for a given $\theta_n$ such that

$$(\mathcal{L}_{NS}\mathbf{U}_{NS},\mathcal{L}_{NS}\mathbf{V}_{NS})_{0,\Omega} = (\boldsymbol{\mathcal{G}}_{NS},\mathcal{L}_{NS}\mathbf{V}_{NS})_{0,\Omega}\quad\forall\mathbf{V}_{NS}\in X_{NS}(\Omega), \tag{3.7}$$

where $\mathcal{L}_{NS}$ represents the Navier-Stokes operator, $\boldsymbol{\mathcal{G}}_{NS}$ the corresponding source term. Likewise, it is also possible to write the necessary condition for the energy equation as

Find $\mathrm{U}_E = \theta\in X_E(\Omega)$ for a given $(\rho_n,\boldsymbol{u}_n,\varphi_n)$ such that

$$(\mathcal{L}_E \mathrm{U}_E, \mathcal{L}_E \mathrm{V}_E)_{0,\Omega} = (\mathcal{G}_E, \mathcal{L}_E \mathrm{V}_E)_{0,\Omega} \quad \forall \mathrm{V}_E \in X_E(\Omega), \tag{3.8}$$

where $\mathcal{L}_E$ represents the energy operator, $\mathcal{G}_E$ the corresponding source term. The Newton linearization method is used to cope with the nonlinear terms in the Navier-Stokes equations. For the Navier-Stokes equations in a two-dimensional spatial domain, the set of partial differential equations with the unknowns $\mathbf{U}_K^T = [\rho\ u\ v\ \varphi]$ can be represented as

$$\begin{aligned}\left[\frac{\partial}{\partial t} + u_l\frac{\partial}{\partial x} + v_l\frac{\partial}{\partial y} + \frac{\partial u_l}{\partial x} + \frac{\partial v_l}{\partial y}\right]\rho + \left[\rho_l\frac{\partial}{\partial x} + \frac{\partial \rho_l}{\partial x}\right]u + \left[\rho_l\frac{\partial}{\partial y} + \frac{\partial \rho_l}{\partial y}\right]v \\ = u_l\frac{\partial \rho_l}{\partial x} + \rho_l\frac{\partial u_l}{\partial x} + v_l\frac{\partial \rho_l}{\partial y} + \rho_l\frac{\partial v_l}{\partial y},\end{aligned} \tag{3.9}$$

$$\begin{aligned}&\left[\left(\frac{24}{(3-\rho_l)^2} - 6\rho_l\right)\frac{\partial}{\partial x} + \left(\frac{\partial u_l}{\partial t} + u_l\frac{\partial u_l}{\partial x} + v_l\frac{\partial u_l}{\partial y} - \frac{1}{We}\frac{\partial \varphi_l}{\partial x}\right)\right]\rho \\ &\quad + \left[\rho_l\left(\frac{\partial}{\partial t} + u_l\frac{\partial}{\partial x} + v_l\frac{\partial}{\partial y}\right) - \frac{1}{Re}\left(\frac{4}{3}\frac{\partial^2}{\partial x^2} + \frac{\partial^2}{\partial y^2}\right) + \rho_l\frac{\partial u_l}{\partial x}\right]u \\ &\quad + \left[\rho_l\frac{\partial u_l}{\partial y} - \frac{1}{3Re}\frac{\partial^2}{\partial x \partial y}\right]v - \frac{1}{We}\rho_l\frac{\partial \varphi}{\partial x} \\ &\quad = \rho_l\frac{\partial u_l}{\partial t} + 2\rho_l u_l\frac{\partial u_l}{\partial x} + 2\rho_l v_l\frac{\partial u_l}{\partial y} - \frac{1}{We}\rho_l\frac{\partial \varphi_l}{\partial x} - \frac{8\rho_l}{3-\rho_l}\frac{\partial \theta_n}{\partial x},\end{aligned} \tag{3.10}$$

$$\begin{aligned}&\left[\left(\frac{24}{(3-\rho_l)^2} - 6\rho_l\right)\frac{\partial}{\partial y} + \left(\frac{\partial v_l}{\partial t} + u_l\frac{\partial v_l}{\partial x} + v_l\frac{\partial v_l}{\partial y} - \frac{1}{We}\frac{\partial \varphi_l}{\partial y}\right)\right]\rho + \left[\rho_l\frac{\partial v_l}{\partial x} - \frac{1}{3Re}\frac{\partial^2}{\partial x \partial y}\right]u \\ &\quad + \left[\rho_l\left(\frac{\partial}{\partial t} + u_l\frac{\partial}{\partial x} + v_l\frac{\partial}{\partial y}\right) - \frac{1}{Re}\left(\frac{\partial^2}{\partial x^2} + \frac{4}{3}\frac{\partial^2}{\partial y^2}\right) + \rho_l\frac{\partial v_l}{\partial y}\right]v - \frac{1}{We}\rho_l\frac{\partial \varphi}{\partial y} \\ &\quad = \rho_l\frac{\partial v_l}{\partial t} + 2\rho_l u_l\frac{\partial v_l}{\partial x} + 2\rho_l v_l\frac{\partial v_l}{\partial y} - \frac{1}{We}\rho_l\frac{\partial \varphi_l}{\partial y} - \frac{8\rho_l}{3-\rho_l}\frac{\partial \theta_n}{\partial y},\end{aligned} \tag{3.11}$$

$$\left[\frac{\partial^2}{\partial x^2} + \frac{\partial^2}{\partial y^2}\right]\rho - \varphi = 0. \tag{3.12}$$

The terms with subscript $l$ represent the values from previous iterative steps for linearization. In the same manner, for the energy equation in a two-dimensional domain, the set of partial equations with the unknown $\mathrm{U}_E = \theta$ can be represented as

$$\begin{aligned}&\left[c\rho_n\left(\frac{\partial}{\partial t} + u_n\frac{\partial}{\partial x} + v_n\frac{\partial}{\partial y}\right) + \frac{8\rho_n}{3-\rho_n}\left(u_n\frac{\partial}{\partial x} + v_n\frac{\partial}{\partial y}\right) - k_0\left(\frac{\partial^2}{\partial x^2} + \frac{\partial^2}{\partial y^2}\right)\right. \\ &\quad \left. + \left\{\frac{24}{(3-\rho_n)^2}\left(\frac{\partial \rho_n}{\partial x}u_n + \frac{\partial \rho_n}{\partial y}v_n\right) + \frac{8\rho_n}{3-\rho_n}\left(\frac{\partial u_n}{\partial x} + \frac{\partial v_n}{\partial y}\right)\right\}\right]\theta \\ &\quad = \alpha_n + \beta_n + \gamma_n + \delta_n + \varepsilon_n.\end{aligned} \tag{3.13}$$

For all sets of the equations, the final system with the boundary conditions included can then be expressed as

$$\mathcal{L}\mathbf{U} = \boldsymbol{\mathcal{G}} \quad \text{in } \Omega, \tag{3.14}$$

$$\mathcal{B}\mathbf{U} = \mathbf{U}_\Gamma \quad \text{on } \Gamma, \tag{3.15}$$

where $\mathcal{B}$ represents the boundary conditions operator and $\mathbf{U}_\Gamma$ the specified values on the boundaries. In this work, the boundary conditions are incorporated into the least-squares functional so that they are also a part of the minimization problem, namely

$$\mathcal{J}(\mathbf{U}) = \frac{1}{2}\|\mathcal{L}\mathbf{U} - \boldsymbol{\mathcal{G}}\|_{0,\Omega}^2 + \frac{1}{2}\|\mathcal{B}\mathbf{U} - \mathbf{U}_\Gamma\|_{0,\Gamma}^2, \tag{3.16}$$

or equivalently,

Find $\mathbf{U} \in X(\Omega)$ such that

$$\mathcal{A}(\mathbf{U}, \mathbf{V}) = \mathcal{F}(\mathbf{V}) \quad \forall \mathbf{V} \in X(\Omega), \tag{3.17}$$

with

$$\mathcal{A}(\mathbf{U}, \mathbf{V}) = (\mathcal{L}\mathbf{U}, \mathcal{L}\mathbf{V})_{0,\Omega} + (\mathcal{B}\mathbf{U}, \mathcal{B}\mathbf{V})_{0,\Gamma}, \tag{3.18}$$

$$\mathcal{F}(\mathbf{V}) = (\boldsymbol{\mathcal{G}}, \mathcal{L}\mathbf{V})_{0,\Omega} + (\mathbf{U}_\Gamma, \mathcal{B}\mathbf{V})_{0,\Gamma}, \tag{3.19}$$

where $\mathcal{A}: X \times X \to \mathbb{R}$ is a symmetric, positive definite bilinear form and $\mathcal{F}: X \to \mathbb{R}$ is a continuous linear form.

The inclusion of the boundary residual allows the use of spaces $X(\Omega)$ that are not constrained to satisfy the boundary conditions. If the boundary terms are omitted, the boundary conditions must be strongly enforced in the definition of the space $X(\Omega)$. Restricting the variational problem (3.17) to a finite dimensional space $X_h(\Omega)$, i.e., $\mathbf{U}_h \in X_h(\Omega) \subset X(\Omega)$, the least-squares formulation can be stated as

Find $\mathbf{U}_h \in X_h(\Omega)$ such that

$$\mathcal{A}(\mathbf{U}_h, \mathbf{V}_h) = \mathcal{F}(\mathbf{V}_h) \quad \forall \mathbf{V}_h \in X_h(\Omega). \tag{3.20}$$

Both nonlinear and decoupling convergences are declared when the relative norm of the residual, i.e., $\|\Delta\mathcal{R}\|_0/\|\mathcal{R}\|_0$, is less than $10^{-6}$, with the residual defined as

$$\|\mathcal{R}\|_{0,\Omega}^2 = \int [\mathcal{L}\mathbf{U}_h - \boldsymbol{\mathcal{G}}]^2 \, d\Omega. \tag{3.21}$$

*3.2. Spectral element discretization*

The computational domain $\Omega$ is divided into $Ne$ non-overlapping sub-domains $\Omega_e$ such that

$$\Omega = \sum_{e=1}^{Ne} \Omega_e \quad \Omega_i \cap \Omega_j = \emptyset, \quad i \neq j. \tag{3.22}$$

A time-space coupled formulation with the time-stepping procedure is used, i.e., the transient solution is approximated on consecutively aligned space-time strips, and a strip is composed of only one element in time, $\Omega_e = \Omega_e^x \times \Omega_e^t = (\boldsymbol{x}_e, \boldsymbol{x}_{e+1}) \times (t_n, t_{n+1})$ with the time step size $\Delta t = t_{n+1} - t_n$. By an invertible mapping, each subdomain is mapped onto the unit cube $(\xi, \varsigma, \eta) = [-1,1]^3$ for a two-dimensional spatial domain. This time-stepping scheme is unconditionally stable, but the accuracy depends on $\Delta t$ [21].

The use of higher continuity discretization in the least-squares method has shown a significant improvement in the accuracy of evolutions for Riemann shock tube problem [22]. In order to describe the interfacial solution with high gradient, $C^1$ $p$-version hierarchical approximation functions, particularly Hermite polynomials, are used to approximate the local solution in each element $\Omega_e$, $\boldsymbol{u}_e^h$. A basis function for a two-dimensional space and time domain can be written as a tensor product of one-dimensional basis functions with the same order, i.e., $\boldsymbol{\Phi}^m(\xi, \varsigma, \eta) = \phi_i(\xi) \otimes \phi_j(\varsigma) \otimes \phi_k(\eta)$, with $m = i + j(p+1) + k(p+1)^2$ where $0 \leq i, j, k \leq p$. Thus, the local approximation $\boldsymbol{u}_e^h$ can be expressed in a linear combination of $\boldsymbol{\Phi}^m$ as

$$\boldsymbol{u}_e^h = \sum_{m=1}^{(p+1)^3} \mathrm{U}_e^m \boldsymbol{\Phi}_e^m, \tag{3.23}$$

with the expansion coefficient $\mathrm{U}_e^m$. The same basis functions and construction approach have been used in our previous study [23-24].

The assembly matrix in an element level can be written as

$$\boldsymbol{\mathcal{A}}_e = \int_{\Omega_e} [\mathcal{L}(\boldsymbol{\Phi}_0) \dots \mathcal{L}(\boldsymbol{\Phi}_{Ne-1})]^T [\mathcal{L}(\boldsymbol{\Phi}_0) \dots \mathcal{L}(\boldsymbol{\Phi}_{Ne-1})] d\Omega_e, \tag{3.24}$$

$$\boldsymbol{\mathcal{F}}_e = \int_{\Omega_e} [\mathcal{L}(\boldsymbol{\Phi}_0) \dots \mathcal{L}(\boldsymbol{\Phi}_{Ne-1})]^T \boldsymbol{\mathcal{G}} d\Omega_e. \tag{3.25}$$

The Gaussian rule on the GLL-roots are used for the numerical integration, and larger number of quadrature points $Q$ than the expansion order $p$, $Q = p + 3$, is used to improve the convergence rate of the solution [25].

The conjugated gradient method with the Jacobi preconditioner is used to solve the algebraic equation. A Matlab code and Matlab MPI are developed at our group as the main setup and for parallel computing. The global approximation $\boldsymbol{u}^h$ are constructed by a combination of the local approximations $\boldsymbol{u}_e^h$ as

$$\boldsymbol{u}^h = \bigcup_{e=1}^{Ne} \boldsymbol{u}_e^h. \tag{3.26}$$

## 4. Convergence analysis based on the manufactured solution

In order to verify our solver, the following manufactured solution for the thermal NSK equations, expressed as products of trigonometrical functions, is used:

$$\begin{aligned} \rho(x,y,t) &= 1.0647 + 0.7453 \sin(\pi x) \sin(\pi y) \cos(\pi t), \\ u(x,y,t) &= \cos(\pi x) \sin(\pi y) \cos(\pi t), \\ v(x,y,t) &= -\sin(\pi x) \cos(\pi y) \cos(\pi t), \\ \theta(x,y,t) &= 0.85 + 0.1 \sin(\pi x) \sin(\pi y) \sin(\pi t). \end{aligned} \tag{4.1}$$

The extrema of the density solution are set to be the densities of bulk phases at $\theta = 0.85$ to assure the stability of the equilibrium state. The corresponding force terms to the manufactured solution are added to the right-hand side of the discretized equations. The initial and boundary conditions are given by the manufactured solution; Dirichlet boundary conditions for the velocities and temperature and Neumann boundary condition for the density. The $L^2$-norm of the difference between the approximated solution $\mathbf{U}_h$ and the manufactured solution $\mathbf{U}_m$, i.e., $\|\mathbf{U}_h - \mathbf{U}_m\|_{0,\Omega}$ is chosen as an error indicator, and it is written as

$$\|\mathbf{U}_h - \mathbf{U}_m\|_{0,\Omega}^2 = \int [\mathbf{U}_h - \mathbf{U}_m]^2 \, d\Omega. \tag{4.2}$$

The governing equations are solved over a domain $\Omega_{\boldsymbol{x}} = [0,1]^2$ and a single element time slab with $\Delta t = 0.05$, until $t = 5.0$ (2.5 periods). The Courant-Friedrich-Lewy (CFL) condition is used to define the time-step

size:

$$\Delta t = \frac{\mathrm{CFL}\times h}{U_0}, \tag{4.3}$$

where the stable time-step size is generated as CFL $< 1$. In the verification study, the CFL ranges from 0.25 to 0.75 with $U_0$ of 0.5.

Figure 2 presents the errors in time for the number of spatial elements $Ne = 15^2$ and the expansion order of $p = 3$, and the errors at $t = 5.0$ from the $h$-refinement study of $Ne = 10^2, 15^2, 20^2, 25^2, 30^2$ and with $p = 3$. The errors oscillate in time depending on the solution values, but the amplitudes of the oscillation are stable. The errors in the $h$-refinement study show the expected linear convergence with slope 4, as theoretically predicted for a fixed expansion order $p = 3$.

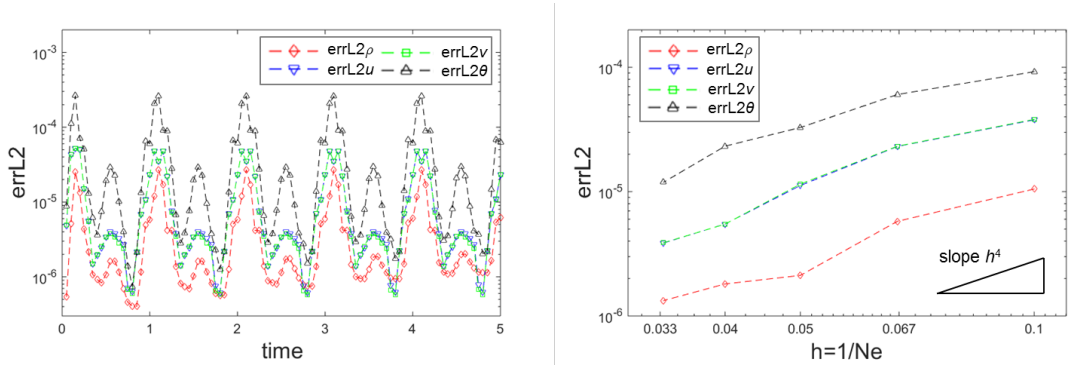


Figure 2. Errors in time with $Ne = 15^2$ and $p = 3$ (left) and $h$-refinement study of $Ne = 10^2, 15^2, 20^2, 25^2, 30^2$ with $p = 3$ (right), manufactured solution.

## 5. Numerical examples

We validate the implemented code with two numerical examples: evaporation/condensation of a single bubble and thermocapillary convection. For all simulations, the initial condition for the density is given as close to the profile at the equilibrium state, and it is expressed as

$$\rho_0 = \frac{\rho_l + \rho_v}{2} + \frac{\rho_l - \rho_v}{2}\tanh\left(\frac{z}{2}\sqrt{We}\right), \tag{5.1}$$

for bulk liquid density $\rho_l$ and bulk vapor density $\rho_v$, and with the z-coordinate chosen along the gradient of density. This hyperbolic function is used as the initial profile in many numerical examples [13-15, 17]. In our previous work [17], the bulk densities at each temperature were estimated, and they are presented in Table 1. The densities were obtained by the equal area rule [15], and the equilibrium states at corresponding temperature were confirmed by our solver.

Table.1 The liquid and vapor densities at the equilibrium state at different temperatures.

| $\theta$ | 0.80 | 0.85 | 0.90 | 0.95 |
|---|---|---|---|---|

| | | | | |
|---|---|---|---|---|
| $\rho_l$ | 1.932 | 1.810 | 1.656 | 1.463 |
| $\rho_v$ | 0.2397 | 0.3194 | 0.4244 | 0.5806 |

*5.1. Evaporation and condensation of a single bubble*

In this example, a single bubble with a radius of 0.25 is located at the center of the computational domain $[0,1]^2$, and it is evaporated or condensed by constant wall temperature. Initially the entire domain is at the equilibrium state with $\theta_0 = 0.85$, corresponding bulk densities $\rho_l = 1.810$ and $\rho_v = 0.3194$, and four different cases with $0.80, 0.85, 0.90, 0.95$ of wall temperatures are considered. The simulation parameters we used here are $Ne = 20^2, p = 4, \Delta t = 0.05, Re = 1000, We = 4000, k_0 = 1$ and $c = 1$. The simulations run until they reach their equilibrium states, and the equilibrium state is declared when $L^\infty$-norm of maximum difference of pointwise density between the current time step and the previous time step is lower than $10^{-4}$, i.e., $max(\rho_n - \rho_{n-1}) < 10^{-4}$.

The radius of single bubble at the equilibrium state can be predicted analytically as follows: with the initial equilibrium state at $\theta_0 = 0.85$ and the initial bubble radius of $0.25$, the total mass $\mathcal{M}$ can be calculated as $\mathcal{M} = \rho_v \times \pi \times 0.25^2 + \rho_l \times (1 - \pi \times 0.25^2)$. With the total mass maintained constant, the radius of the bubble at the equilibrium state, denoted as $R_e$, can be estimated with the same equation but with different bulk densities for each wall temperature, by assuming that the equilibrium temperature is equal to the wall temperature. Together with $R_e$, the radius of the bubble from our simulations, denoted as $R_s$, are presented in Table 2. The equilibrium radii have close agreement with the estimated radii, and for $\theta = 0.95$ only liquid phase is left. The density profiles for each wall temperature are given in Figure 3. Our results also have good agreement with the results from [26]. This example shows that our solver provides the result with stable equilibrium states and the mass conservation.

Table 2. Estimated bulk densities and radius of evaporating/condensing bubble at equilibrium state.

| $\theta$ | $\rho_l$ | $\rho_v$ | $R_s$ | $R_e$ |
|---|---|---|---|---|
| 0.80 | 1.932 | 0.2397 | 0.2793 | 0.2791 |
| 0.85 | 1.810 | 0.3194 | 0.2500 | 0.2500 |
| 0.90 | 1.656 | 0.4244 | 0.1893 | 0.1906 |
| 0.95 | 1.463 | 0.5806 | - | - |

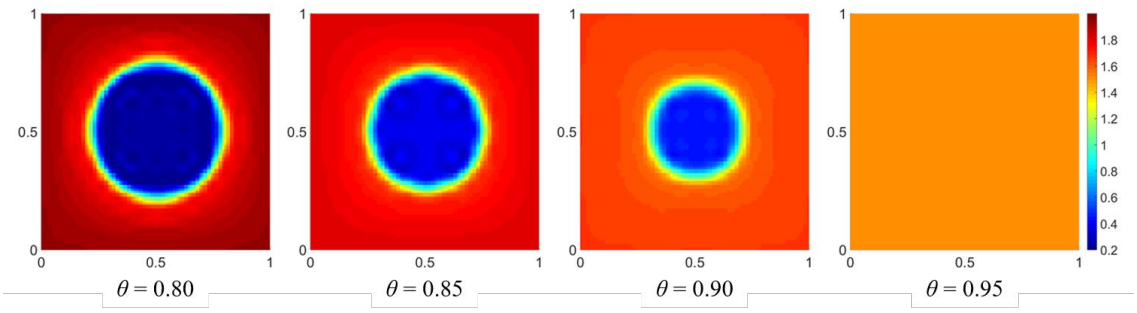


Figure 3. Density profiles of evaporating/condensing single bubble for each wall temperature.

*5.2. Thermocapillary convection*

The Marangoni effect is induced by surface tension gradient at the interface between two fluids. Among many forces inducing the Marangoni effect, the temperature gradient can be one of them in such a way that the increase of local temperature increases surface tension, and then the imbalance of surface tension drives the bubble toward higher temperature. This motion due to the temperature gradient is referred to as the thermocapillary convection or Benard-Marangoni convection [27]. Such convection is critical in understanding welding, crystal growth and electron beam melting.

Initially a single bubble with a radius of 0.25 is located at the center of a square domain $\Omega_x = [0,1]^2$. The initial condition and the boundary condition for the velocity field are fixed to zero. The initial equilibrium temperature is set to $\theta_0 = 0.85$. The top and bottom walls are insulated, i.e., $\partial\theta/\partial y = 0$, and on the left and right walls the temperature is fixed to 0.85 and 0.90, respectively. The mesh size is taken to be $h = 0.025$ with $Ne = 40^2$ and $p = 4$. The time step size is set to $\Delta t = 0.025$, corresponding to unity CFL. The Reynold number and the flow properties are chosen as $Re = 1000$, $k_0 = 1$ and $c = 1$. We vary the Weber number as $We = 2000, 4000$ and $8000$ to investigate the effect of this parameter.

Figure 4 shows the evolution of temperature for $We = 2000$ and the velocity field with the interface line, located as the points with density equal to the average density $\rho = (\rho_l + \rho_v)/2$, are, for $We = 2000, 4000$ and $8000$. Note that for $We = 2000$ data at $t = 0.05, 4.5$ and $9.0$ are presented with the data for $We = 4000$ with two times longer time intervals, at $t = 0.1, 9.0$ and $18.0$ and for $We = 8000$ with four times longer time intervals, at $t = 0.2, 18.0$ and $36.0$. In all three cases the bubble moves in the positive thermal gradient direction. We can also see the motion with $We = 2000$ is two times and four times faster than the one with $We = 4000$ and $We = 8000$, respectively. Thus, it can be concluded that the speed induced by thermocapillary convection is proportional to $We^{-1}$. Since the same time step size is used for each simulation case and the reference values, presented in (2.24), are based on the fluid properties, we can see the surface tension $\sigma$ is proportional to $We^{-1}$ with the definition of the Weber number in (2.25). Therefore, we can conclude the bubble speed induced by the thermocapillary convection is proportional to the surface tension in our simulation, and this result can be demonstrated by the experimental study of [28] - the steady state velocity of a spherical drop in a constant temperature gradient field for two fluids of equal thermal conductivity is proportional to the surface tension.

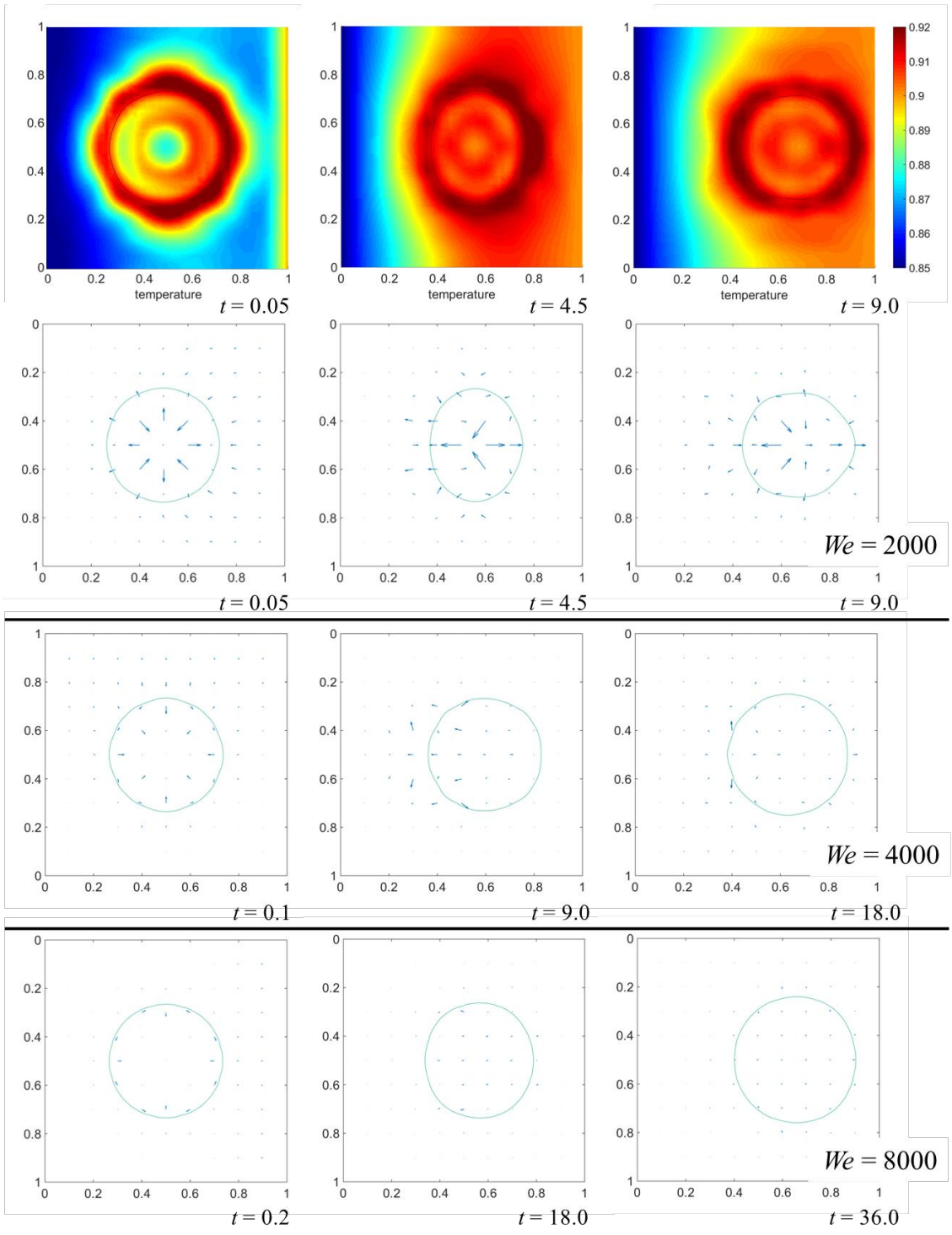


Figure 4. Evolution of density and temperature of $We = 2000$ and the velocity fields with interface line ($\rho = 1.0647$) of $We = 2000$ and $8000$. $We = 2000$ is at $t = 0.05, 4.5$ and $9.0$, and $We = 8000$ is at $t = 0.2, 18.0$ and $36.0$.

## 6. Conclusion

We presented the least-squares spectral element scheme for thermal Navier-Stokes-Korteweg (NSK) system. The equations were recast as the second order PDEs to be approximated by $C^1$ Hermite polynomials, and rewritten along with the least-squares formulation. A time-stepping procedure, Newton linearization and the element-by-element technique were implemented. The convergence analysis based on manufactured solution was conducted to verify our solver. It is confirmed that our solver follows the van der Waals fluid model with an example of the evaporation and condensation of a single bubble by showing the equilibrium state is close enough to the theoretically predicted state. Thermocapillary convection was handled with our solver. The imbalance of surface tension due to the temperature gradient drove the bubble toward higher temperature, and the effect of the surface tension on traveling speed was demonstrated by validation with experimental observations from the literature.

**Acknowledgements**

This work was supported by the Research Council of Norway (FRINATEK project 214424), Norway.

**References**

[1] J. Kim, A diffuse-interface model for axisymmetric immiscible two-phase flow, Appl. Math. Comput. 160.2 (2005) 589-606.

[2] S. Gross, A. Reusken, Numerical methods for two-phase incompressible flows, Springer Science & Business Media, New York, 2011.

[3] M. Fernandino, C.A. Dorao, The least squares spectral element method for the Cahn–Hilliard equation, Applied Mathematical Modelling, Appl. Math. Model. 35.2 (2011) 797-806.

[4] A. Pecenko, J.G.M. Van Deurzen, J.G.M. Kuerten, C.W.M. Van der Geld, Non-isothermal two-phase flow with a diffuse-interface model, Int. J. Multiphas. Flow. 37.2 (2011) 149-165.

[5] P. Yue, J.J. Feng, C. Liu, J. Shen, A diffuse-interface method for simulating two-phase flows of complex fluids, J. Fluid Mech. 515 (2004) 293-317.

[6] P.M. Dupuy, Y. Lin, M. Fernandino, H.A. Jakobsen, H.F. Svendsen, Modelling of high pressure binary droplet collisions, Compu. Math. Appl. 61.12 (2011) 3564-3576.

[7] J.A. Warren, W.J. Boettinger, Prediction of dendritic growth and microsegregation patterns in a binary alloy using the phase-field method, Acta Metall. Mater. 43.2 (1995) 689-703.

[8] J.T. Oden, A. Hawkins, S. Prudhomme, General diffuse-interface theories and an approach to predictive tumor growth modeling, Math. Mod. Meth. Appl. S. 20.3 (2010) 477-517.

[9] D.J. Korteweg (1901), Sur la forme que prennent les équations du mouvement des fluides si l'on tient compte des forces capillaires causées par des variations de densité considérables mais continues et sur la théorie de la capillarité dans l'hypothese d'une variation continue de la densité, Archives Néerlandaises des Sciences exactes et naturelles, 6.1 (1901).

[10] J.E. Dunn, J. Serrin, On the thermomechanics of interstitial working, In The Breadth and Depth of Continuum Mechanics, Springer Berlin Heidelberg, Germany (1986) pp. 705-743.

[11] A. Onuki, Dynamics van der Waals theory, Physical Review E, 75.3 (2007) 036304.

[12] A. Pecenko, J.G.M. Kuerten, C.W.M. Van der Geld, A diffuse-interface approach to two-phase isothermal flow of a Van der Waals fluid near the critical point, Int. J. Multiph. Flow, 36.7 (2010) 558-569.

[13] J. Liu, H. Gomez, J.A. Evans, T.J. Hughes, C.M. Landis, Functional entropy variables: a new methodology for deriving thermodynamically consistent algorithms for complex fluids, with particular reference to the isothermal Navier–Stokes–Korteweg equations, J. Comput. Phys. 248 (2013) 47-86.

[14] L. Tian, Y. Xu, J.G.M. Kuerten, J.J.W. Van der Vegt, A local discontinuous Galerkin method for the (non)-isothermal Navier–Stokes–Korteweg equations, J. Comput. Phys. 295 (2015) 685-714.

[15] D. Diehl, J. Kremser, D. Kröner, C. Rohde, Numerical solution of Navier–Stokes–Korteweg systems by Local Discontinuous Galerkin methods in multiple space dimensions, Appl. Math. Comput. 272 (2016) 309-335.

[16] J. Giesselmann, C. Makridakis, T. Pryer, Energy consistent discontinuous Galerkin methods for the Navier–Stokes–Korteweg system, Math. Comp. 83.289 (2014) 2071-2099.

[17] K. Park, M. Fernandino, C.A. Dorao, M. Gerritsma, The least-squares spectral element method for phase-field models for isothermal fluid mixture, accepted for publication in Comput. Math. Appl.

[18] J.S. Rowlinson, Translation of J.D. van der Waals' The thermodynamic theory of capillarity under the hypothesis of a continuous variation of density, J. Stat. Phys. 20 (1979) 200–244.

[19] W.J. Thompson, L.F. Cook, Angular Momentum: An Illustrated Guide to Rotational Symmetries for Physical Systems, Am. J. Phys. 63.7 (1995) 670-671.

[20] D.M. Anderson, G.B. McFadden, A.A. Wheeler, Diffuse-interface methods in fluid mechanics, Annu. Rev. Fluid Mech. 30.1 (1998) 139-165.

[21] J.P. Pontaza, A least-squares finite element formulation for unsteady incompressible flows with improved velocity–pressure coupling, J. Comput. Phys. 217.2 (2006) 563-588.

[22] K.S. Surana, S. Allu, P.W. Tenpas, J.N. Reddy, k-version of finite element method in gas dynamics: higher-order global differentiability numerical solutions, Int. J. Numer. Meth. Eng. 69.6 (2007) 1109-1157.

[23] K. Park, C.A. Dorao, M. Fernandino, Numerical solution of coupled Cahn-Hilliard and Navier-Stokes system using the least-squares spectral element method, In Proceeding of the ICNMM conference, Washington, 2016.

[24] K. Park, M. Fernandino, C.A. Dorao, Numerical solution of incompressible Cahn-Hilliard and Navier-Stokes system with large density and viscosity ratio using the least-squares spectral element method, J. Fluid Flow Heat Mass. 3.1 (2016) 73-85.

[25] B.D. Maerschalck, M.I. Gerritsma, Higher-order Gauss–Lobatto integration for non-linear hyperbolic equations, SIAM J. Sci. Comput. 27.1 (2006) 201-214.

[26] J. Liu, Thermodynamically consistent modeling and simulation of multiphase flow, PhD dissertation, The University of Texas at Austin, 2014.

[27] A.V. Getling, Rayleigh-Benard convection, structures and dynamics, World Scientific, 11, 1998.

[28] N.O. Young, J.S. Goldstein, M.J. Block, The motion of bubbles in a vertical temperature gradient, J. Fluid Mech. 6.3 (1959) 350-356.